Passive wireless antenna sensor for strain and crack sensing – electromagnetic modeling, simulation, and testing

Xiaohua Yi [a], Chunhee Cho [a], James Cooper [b],
Yang Wang [a], Manos M. Tentzeris [b], Roberto T. Leon [c]

[a] School of Civil and Environmental Engineering, Georgia Institute of Technology, Atlanta, GA 30332, USA
[b] School of Electrical and Computer Engineering, Georgia Institute of Technology, Atlanta, GA 30332, USA
[c] Department of Civil and Environmental Engineering, Virginia Polytechnic Institute and State University, Blacksburg, VA 24061, USA

Abstract

This research investigates a passive wireless antenna sensor designed for strain and crack sensing. When the antenna experiences deformation, antenna shape changes, causing shift in electromagnetic resonance frequency of the antenna. A radio frequency identification (RFID) chip is adopted for antenna signal modulation, so that a wireless reader can easily distinguish backscattered sensor signal from unwanted environmental reflections. The RFID chip captures its operating power from interrogation electromagnetic wave emitted by the reader, which allows the antenna sensor to be passive (battery-free). This paper first reports the latest simulation results on radiation patterns, surface current density, and electromagnetic field distribution. The simulation results are followed with experimental results on the strain and crack sensing performance of the antenna sensor. Tensile tests show that the wireless antenna sensor can detect small strain changes lower than 20 με, and can perform well at large strains higher than 10,000 με. With a high-gain reader antenna, the wireless interrogation distance can be increased up to 2.1 m. Furthermore, an array of antenna sensors is capable of measuring strain distribution in close proximity. During emulated crack and fatigue crack

tests, the antenna sensor is able to detect the growth of a small crack.

Keywords: folded patch antenna; wireless passive sensor; strain sensing; crack sensing; RFID

1. Introduction

In order to accurately assess deterioration of civil, mechanical, and aerospace structures, a large volume of research in structural health monitoring (SHM) has been inspired over past few decades[1]. SHM systems can advance time-based maintenance into more cost effective condition-based maintenance. Sensors have been developed to measure various structural responses and operating conditions, including strain, displacement, acceleration, humidity, temperature, etc. Among the measurements, strain can be an important indicator for stress concentration and crack development. Metal foil strain gages are currently among the most common solutions for strain measurement, owing to their low-cost, simple circuitry, and acceptable reliability in many applications. However, when applied to large structures, traditional metal foil strain gages require lengthy cable connections for power supply and data acquisition, which can significantly increase installation time and system cost [2].

Among many new SHM technologies, wireless sensing can help to significantly reduce instrumentation time and system cost [3-6]. An exhaustive review on wireless sensing for SHM can be found in [7], which summarizes development of various academic and industrial wireless sensing devices. A wireless sensing device usually has three functional modules: sensing interface (e.g. converting analog sensor signal to digital data), computing core (data storage and processing), and wireless transceiver (digital communication with peers or a wireless gateway server). To obtain

different types of measurements, various sensors can be connected with the sensing interface of a wireless sensing device. For example, strain measurement is obtained by interfacing the device with a metal foil strain gage. In addition, current wireless sensing devices usually operate on external power source, such as batteries.

To avoid periodic expensive battery replacement in the field, rechargeable batteries are usually deployed. These batteries are charged by an integrated energy harvester. Possible sources for energy harvesting include solar energy, mechanical vibration, thermal gradients, etc [8]. However, even with a reliable source for energy harvesting, rechargeable batteries usually have a limited life span. To resolve this difficulty, one alternative approach is to adopt radiofrequency identification (RFID) technology for passive wireless sensing [9]. An RFID-based wireless sensor can capture operation power from interrogation by a wireless reader. For example, a WISP (wireless interrogation and sensing platform) unit receives operation power from an ultra-high frequency (UHF) RFID reader, and communicates with the reader through RFID interface [10]. Nevertheless, a WISP unit still contains a programmable microcontroller and an analog-to-digital converter, which makes its basic architecture close to traditional wireless sensing devices as summarized in [7].

Some other wireless passive strain sensors have also been proposed based on inductive coupling that involves two adjacent inductors [11-13]. The interrogation distance achieved by inductive coupling is usually limited to several inches, which is inconvenient for practical applications. Similarly, a circular patch antenna sensor has been proposed for omnidirectional strain sensing by wirelessly measuring scattering parameter in the near field of a horn antenna [14]. Since no signal modulation is used by the sensor, the wirelessly received sensor signal is mixed with background reflection, and the sensor also has very limited interrogation distance. In order to increase

interrogation distance, electromagnetic backscattering techniques have been exploited for wireless strain sensing. Since the electromagnetic resonance frequency of an antenna is related to the antenna's physical dimension, the resonance frequency changes when the antenna experiences strain. After bonding or embedding the antenna to a structure, this relationship between resonance frequency and strain can be used for stress/strain measurement. For example, a patch antenna has been designed for wireless strain sensing [15, 16], where a phototransistor is adopted for modulating the RF signal backscattered from the antenna sensor. As a result of the modulation, backscattered sensor signal can be distinguished from environmental reflections. However, besides requiring line of sight, the light-switching mechanism is not practical for outdoor application, where light intensity is usually so strong that the phototransistor is constantly activated and thus, loses ability of switching. As another example, Thomson *et al*. [17] developed an RF cavity sensor for wireless strain sensing. An external antenna needs to be connected with the cavity sensor for interrogation. Due to the cavity configuration, the sensor is likely more suitable for embedment inside concrete, instead of installation on a metallic surface.

To distinguish backscattered sensor signal from unwanted background reflection, researchers have investigated RFID modulation with an antenna sensor. A small-size meander-line antenna with RFID modulation is designed for wireless strain sensing on non-metallic structures [18], although the demonstrated measurable strain resolutions are unlikely enough for most SHM applications. Recently, the authors developed a folded patch antenna for passive wireless strain sensing, which utilizes an inexpensive off-the-shelf RFID chip for signal modulation [19]. The folded patch antenna format is adopted to improve the interrogation distance of the sensor on metallic surface. Strain sensing performance of the antenna sensor was investigated at 0.3 m and 0.6 m interrogation distances.

Tensile test results demonstrate consistent and accurate strain sensing capabilities. The authors further studied the substrate thickness effect on strain sensing performance of the RFID antenna sensor [20]. The tensile test results show that longer interrogation distance can be achieved with thicker substrate. Furthermore, Yi *et al.* [21] studied the thermal effect on strain sensing of the RFID antenna sensor and thus corresponding thermal reduction methods. To thoroughly evaluate the prototype antenna sensor, this paper first presents detailed electromagnetic simulation results for the prototype sensor, such as current density, electromagnetic field distribution, and radiation patterns. Extensive experiments are conducted to investigate the strain sensing capabilities of the prototype sensor, such as sensing resolution, measurement range, sensing consistency at different distances, and strain sensing by a sensor array. Furthermore, to evaluate crack sensing capability of the prototype sensor, emulated crack test is first conducted. A crack testing device is designed to generate milli-meter crack opening. Finally, fatigue crack sensing performance of the prototype sensor is evaluated.

The rest of this paper is organized as follows. Section 2 briefly reviews sensing mechanism of the folded patch antenna sensor. Electromagnetic simulation results for strain sensing are presented. Section 3 describes tensile test results on strain sensing resolution, strain measurement range, strain sensing consistency at large interrogation distances, and strain sensing by an antenna sensor array. Section 4 presents results for emulated crack sensing and fatigue crack sensing. The last section provides a summary and discussion of this work.

2. Design and simulation of the RFID folded patch antenna sensor

This section is organized as follows. Section 2.1 first reviews the design and strain sensing mechanism of an RFID folded patch antenna sensor. Section 2.2 presents electromagnetic simulation

to evaluate the strain effect of the prototype antenna sensor. The last subsection presents the interrogation power threshold method and corresponding measurement setup.

2.1 Sensor design

Fig. 1 provides a 3D illustration of the prototype RFID antenna sensor design. The front/top side of the sensor contains a thin copper cladding (as conductive part of the antenna) and an RFID chip (SL3ICS1002 from NXP Semiconductors), which are mounted on a 6cm × 6.9cm dielectric substrate. The back/bottom side of the sensor is the electronic ground plane (also made of copper cladding) deposited on the back of the substrate. More detailed description on the antenna sensor can be found in [19].

During the sensor design phase, impedance of the patch antenna is adjusted to match the conjugate of RFID chip impedance. As a result, a smallest amount of power needs to be transmitted from the reader in order to activate the RFID chip. The power reflection coefficient, S_{11}, of the antenna quantifies this transmission efficiency. S_{11} is defined as the ratio of the power reflected by the antenna over the power infused by the RFID chip. A smaller value of S_{11} indicates higher

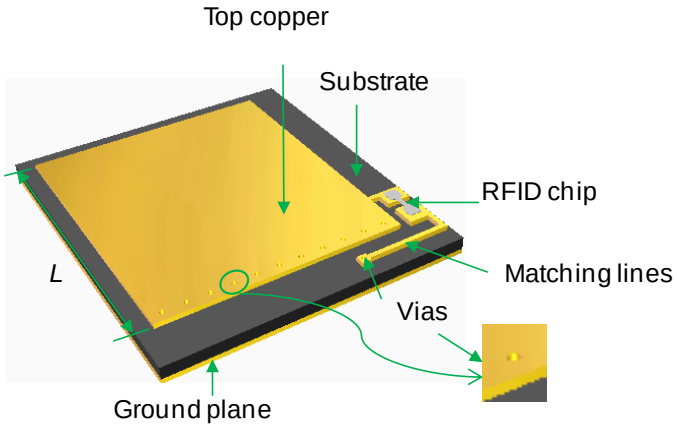

Fig. 1 Illustration of the folded patch antenna sensor (6cm × 6.9cm)

transmission efficiency.

The antenna design is based on a quarter-wave folded-patch topology [9]. When the antenna sensor experiences strain ε in the longitudinal direction, the shifted resonance frequency, f_R, can be estimated as:

$$f_R = \frac{c}{4(1+\varepsilon)(L+\Delta L)\sqrt{\varepsilon_r}} = \frac{f_{R0}}{1+\varepsilon} \approx f_{R0}(1-\varepsilon) \quad (1)$$

where c is the speed of light, L is the physical length of the top copper cladding (5.6cm), ε_r (=2.2 for current design) is the dielectric constant of the substrate, ΔL is the additional electrical length compensation determined by substrate width-to-thickness dimension and dielectric constant. The equation shows that when strain ε is small, resonance frequency of the antenna sensor has an approximately linear relationship with respect to applied strain. This relationship serves as the fundamental mechanism for the wireless strain/crack sensing. The antenna sensor performance for strain sensing is first studied through electromagnetic simulation using a commercial software package, Computer Simulation Technology (CST) Microwave Studio.

2.2 Electromagnetic simulation for strain sensing

Fig. 2 shows the simulation model of the folded patch antenna in CST Microwave Studio. The RFID chip is simulated as a lumped port that has same electrical impedance as the chip. The entire simulation domain is delineated by the cubic box in Fig. 2. The cube is filled with air and the folded patch antenna is located at the cube center. At the outer surfaces of the air cube, boundary condition is set as perfectly matched layer (PML). The PML boundary condition allows electromagnetic wave emitted by the antenna sensor to pass through with minimal reflections, which enables the finite-volume computer model to mimic the dissipation of electromagnetic wave into infinite free

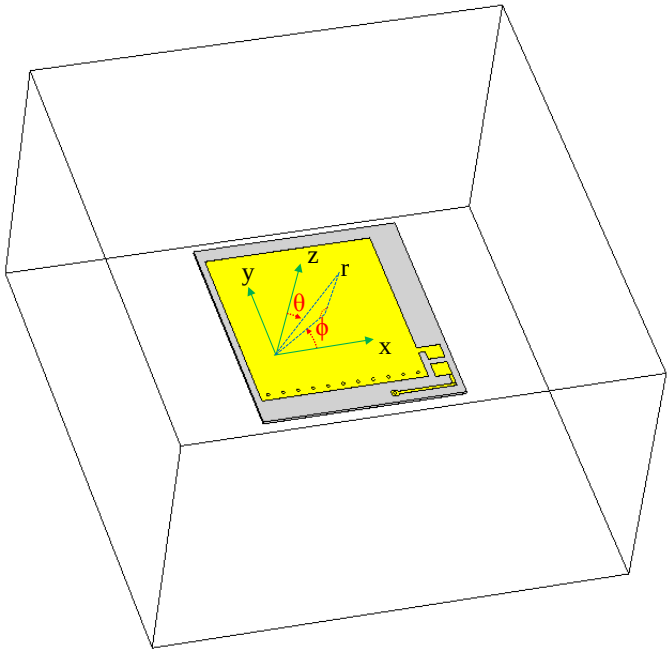

Fig. 2. Simulation model of the folded patch antenna sensor in CST Microwave Studio

space. The copper material in the model is treated as perfect electrical conductor (PEC) boundary condition with zero thickness, which improves computational efficiency. At certain electromagnetic frequency ω, the phasor form of both electric field **E** and magnetic field **H** is described by Helmholtz equation [22]:

$$\nabla^2\mathbf{E} = \mathrm{j}\omega\mu\left(\sigma\mathbf{E} + \mathrm{j}\omega\varepsilon\mathbf{E}\right)$$
$$\nabla^2\mathbf{H} = \mathrm{j}\omega\mu\left(\sigma\mathbf{H} + \mathrm{j}\omega\varepsilon\mathbf{H}\right) \quad (2)$$

where μ, ε, and σ represents material permeability, permittivity, and conductivity, respectively; "j" represents imaginary unit.

During CST simulation, the frequency domain solver is selected due to strong resonance of the antenna sensor. The model contains about 61,000 tetrahedral elements and 409,000 degrees-of-freedom. Within a pre-specified frequency range (905 ~ 920MHz), sensor performance is simulated at every frequency step of 0.01MHz. The total computing time is about 27 minutes. Direct simulation results are electric field **E** and magnetic field **H** in Eq. (2). Based on field distributions, antenna gain $G(\theta, \phi)$ can be estimated as [23]:

$$G(\theta,\phi) \approx 4\pi e_t \frac{\left[\left|E_\theta(\theta,\phi)\right|^2 + \left|E_\phi(\theta,\phi)\right|^2\right]}{\int_{\phi=0}^{2\pi}\int_{\theta=0}^{\pi}\left[\left|E_\theta(\theta,\phi)\right|^2 + \left|E_\phi(\theta,\phi)\right|^2\right]\sin\theta d\theta d\phi} \quad (3)$$

where e_t is the total antenna efficiency, which takes into account losses at the lumped port and within the antenna; E_θ and E_ϕ are far-field electric field components along θ and ϕ directions, respectively. Fig. 3 shows the simulated radiation patterns of the folded patch antenna in **E** plane (ϕ=90˚ in Fig. 3, with electric field) and **H** plane (ϕ=0˚ in Fig. 3, with magnetic field) at resonance frequency 913.623 MHz, respectively. The peak gain of the antenna is -3.54 dB. The half-power beamwidth (HPBW) in **E** and **H** plane are about 129.5˚ and 305˚, respectively. The large HPBW values allow flexible positioning for the interrogation reader antenna.

When a reader illuminates the sensor at certain interrogates frequency (which may or may not equal to antenna resonance frequency), the RFID chip can harvest the energy as long as the interrogation frequency is within the operational range of the chip. The chip then radiates electromagnetic wave back to the reader through the folded patch antenna. An indication of the

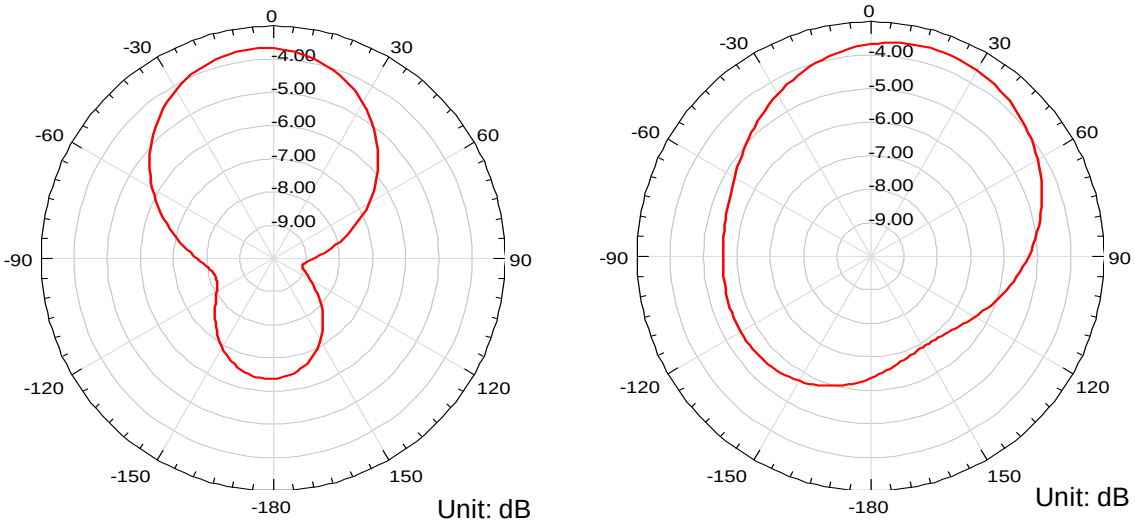

(a) Gain vs θ in **E**-plane (ϕ=90˚) (b) Gain vs θ in **H**-plane (ϕ=0˚)

Fig. 3. Simulated radiation patterns of the folded patch antenna

radiation strength is the density of surface current flowing on the antenna copper surface, at an electromagnetic frequency same as the interrogation signal. Based on simulated magnetic field distribution, the surface current density ($\mathbf{J}_s$) existing at the interface between air and substrate material can be calculated as [22]:

$$\mathbf{J}_s = \nabla \times \left(\mathbf{H}_2 - \mathbf{H}_1 \right) \tag{4}$$

where $\mathbf{H}_1$ and $\mathbf{H}_2$ are the magnetic fields in the two adjacent mediums. If the interface is between copper and air, then $\mathbf{H}_1$ and $\mathbf{H}_2$ are the magnetic fields in the copper and air, respectively. Furthermore, $\mathbf{H}_1$ is zero, since no magnetic field exists inside the copper, which is a perfect conductor. Similarly, if the interface is between Rogers substrate 5880 and air, then $\mathbf{H}_1$ and $\mathbf{H}_2$ are the magnetic fields in the Rogers substrate 5880 and air. Fig. 4(a) and Fig. 4(b) plot the surface current densities in y-direction when the sensor is at zero strain, for two different interrogation frequencies (913.623 MHz and 912 MHz), respectively. Although two figures appear similar, a careful examination reveals that Fig. 4(a)

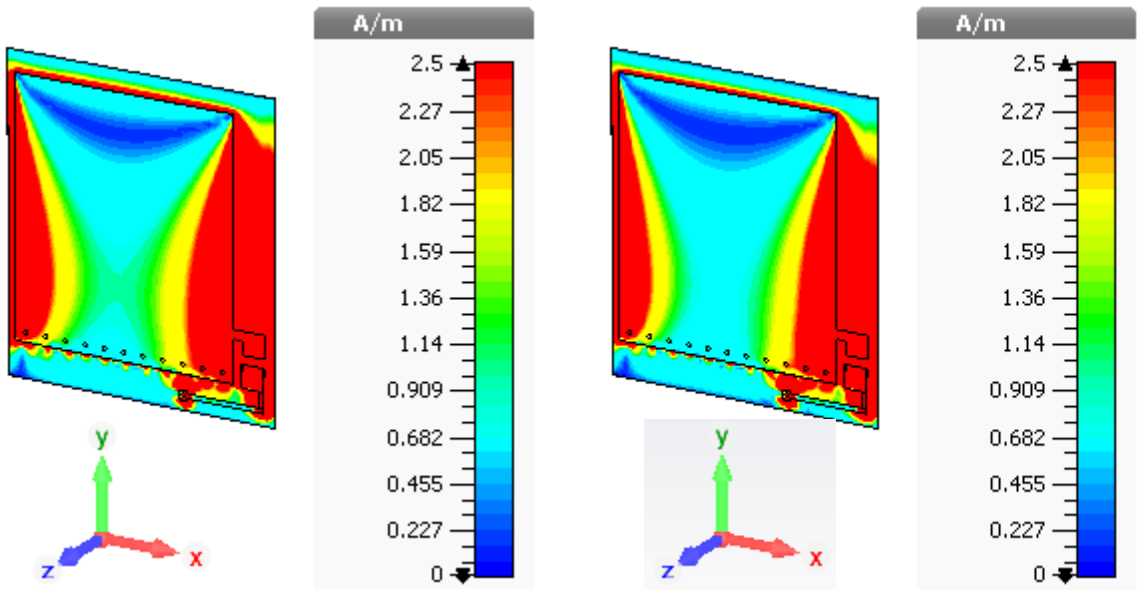

(a) Surface current density at 913.623 MHz (b) Surface current density at 912 MHz

Fig. 4. Simulated surface current densities in y-direction at two different frequencies (0 με)

shows stronger current. In other words, at zero strain, a 913.623 MHz interrogation signal results in stronger antenna sensor radiation than a 912 MHz interrogation signal with the same power level.

After simulating the antenna sensor performance at zero strain level, another simulation is conducted when the antenna deforms at 2,000 με. To simulate the antenna behavior under strain in CST Microwave Studio, sensor dimensions are proportionally scaled, while considering Poisson's ratio. Fig. 5 shows simulated surface current densities at the same two interrogation frequencies, when the antenna is at 2,000 με strain. Opposite to Fig. 4, Fig. 5(a) shows weaker current than Fig. 5(b). In other words, at 2,000 με, a 912 MHz interrogation signal results in stronger antenna sensor radiation than a 913.623 MHz interrogation signal with the same power level.

Furthermore, reflection coefficient (S_{11}) is calculated based on simulated electrical field distribution at the lumped port representing RFID chip [22]:

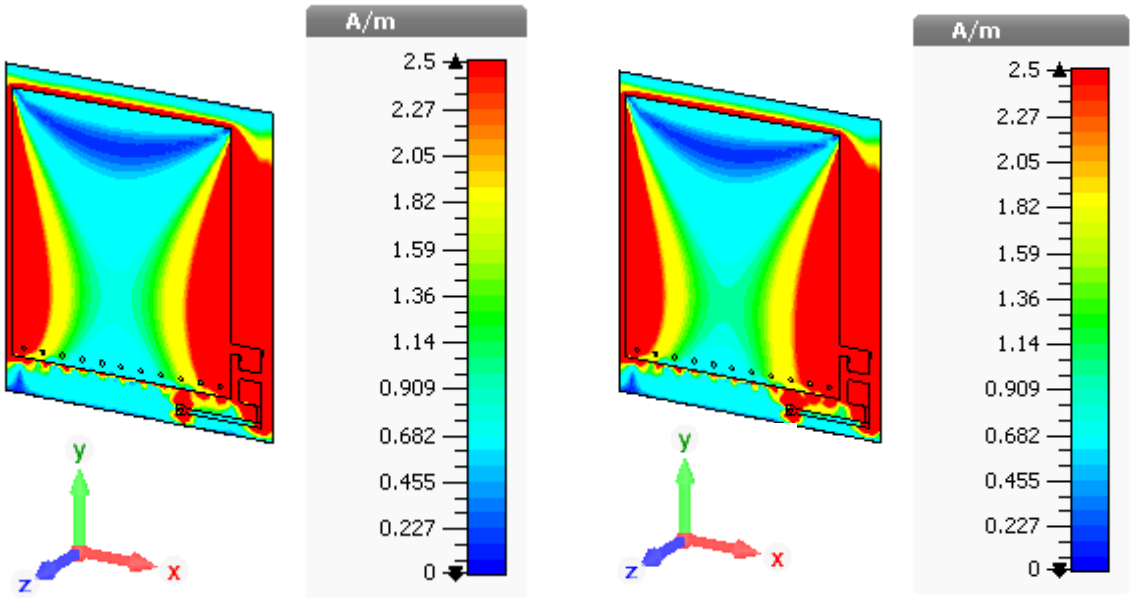

(a) Surface current density at 913.623MHz (b) Surface current density at 912 MHz

Fig. 5. Simulated surface current densities in y-direction at two different frequencies (2,000 με)

$$S_{11} = \frac{V^r}{V^i} \tag{5}$$

where V^i and V^r are equivalent incident and reflected voltages at the port, respectively. S_{11} indicates impedance matching between the lumped port (RFID chip) and the antenna. Smaller S_{11} value means better matching and higher antenna efficiency. Fig. 6(a) shows simulated S_{11} plot of the folded patch antenna sensor at five different strain levels. At each strain level, the antenna resonance frequency is extracted by peak picking. Clear frequency decrease is observed when strain increases. For example, at zero strain level, the antenna resonance frequency is found to be 913.623 MHz. At 2,000 με, the resonance frequency decreases to 912 MHz. The two different resonance frequencies corroborate current density comparison between Fig. 4 and Fig. 5. Stronger surface current occurs when the antenna is excited at resonance frequency, which changes with strain level.

Due to sensor fabrication and installation tolerances in practice, zero-strain resonance frequencies of different pieces of installed antenna sensors can slightly differ. To alleviate the affect on strain measurement, a concept of normalized resonance frequency change is defined. The resonance frequency change is normalized by initial resonance frequency (i.e. f_{R0} at zero strain level) according to following equation:

$$\Delta f_N = \frac{f_R - f_{R0}}{f_{R0}} \approx -\varepsilon \tag{6}$$

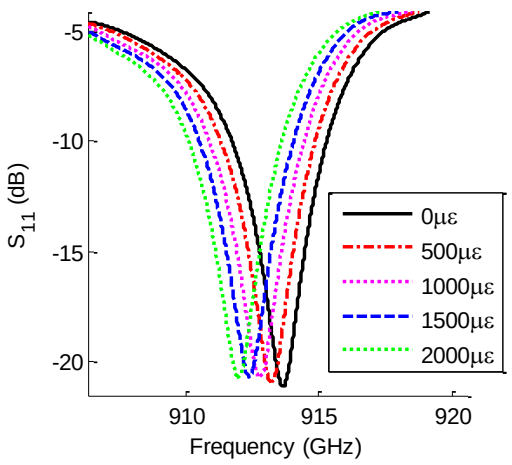

(a) Simulated S_{11} plots at different strain levels

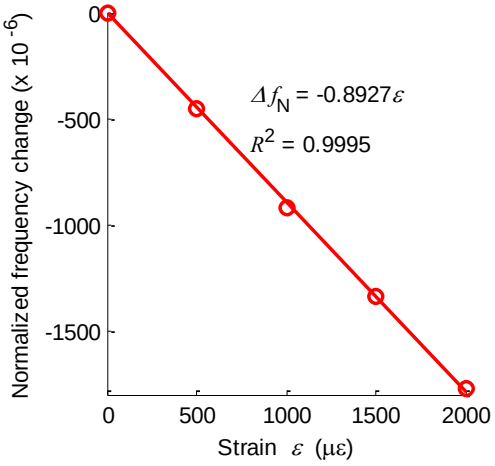

(b) Normalized resonance frequency change Δf_N versus strain ε (f_{R0}=913.623 MHz)

Fig. 6. Simulation results for the folded patch antenna

where Δf_N represents normalized frequency change, and ε is applied strain when the resonance frequency is changed to f_R. Although Eq. (1) shows magnitude of Δf_N approximately equals magnitude of strain ε, in practice, Δf_N usually has a smaller magnitude. The primary reason is that only a percentage of the strain on structural surface is transferred to the top copper layer of the sensor [19]. This strain transfer effect reduces the achieved strain sensitivity:

$$\Delta f_N = -S_N \varepsilon \tag{7}$$

where S_N is the normalized strain sensitivity with a value close to and less than 1.

The resonance frequency at each strain level is extracted from Fig. 6(a) and normalized change is calculated according to Eq. (6). Fig. 6(b) plots the relationship between normalized resonance frequency change and strain. The normalized strain sensitivity is -0.8927 ppm/με, which means 1 με strain experienced by the folded patch antenna introduces 0.8927 ppm (parts per million) decrease in resonance frequency. The normalized strain sensitivity is lower than -1 ppm/με, predicted by Eq. (7). The reason may be partially due to dimensions change of matching lines under strain, which changes

impedance of matching lines and further changes matching between IC chip and the overall patch antenna. The coefficient of determination (R^2) is 0.9995, which indicates a good linearity between normalized frequency change and simulated strain.

2.3 Measurement setup

To distinguish sensor signal from environmental reflection, the RFID chip modulates backscattered signal. Through modulation, a varying pattern is applied to the electromagnetic wave radiated by the antenna sensor. Because environmental reflection has no such variation, the reader can detect the patterned variation in received signal and distinguish modulated backscattering by the sensor. In general, modulation schemes achieve data encoding by regularly switching signal amplitude, phase, or frequency [9]. The modulation schemes used in most RFID systems are amplitude shift keying (ASK) and phase shift keying (PSK). Fig. 7 illustrates the ASK scheme, where signal amplitude is switched between high and low states, representing encoded digital data. The RFID chip performs modulation by rapidly switching chip impedance between two statuses, one closely matched to the antenna impedance and the other one strongly mismatched. The matched status provides a high signal strength, and the mismatched provides a low signal strength, representing two digital states. The

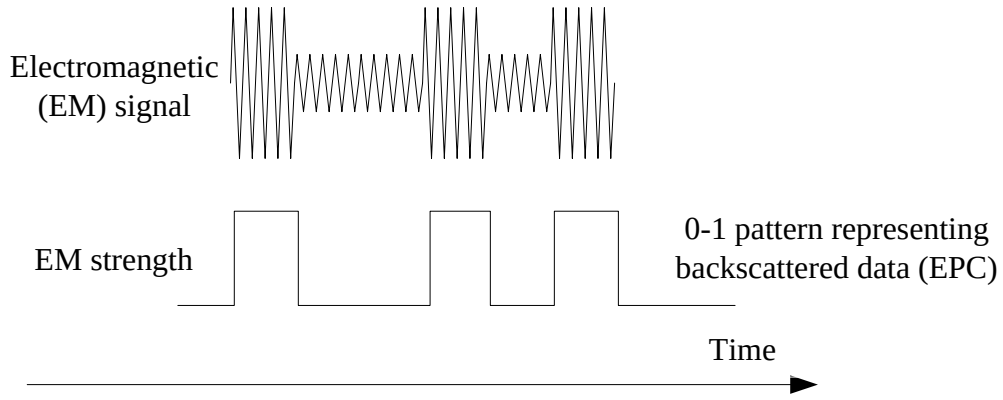

Fig. 7. RFID signal modulation through amplitude shift keying (ASK)

modulation signal is finally received and recognized by the RFID reader [9].

In this study, a Tagformance Lite RFID reader is adopted for interrogation power threshold measurement [24]. The reader can sweep through an interrogation frequency range from 800 MHz to 1000 MHz, with a frequency resolution of 0.1 MHz. At each interrogation frequency, the reader varies the interrogation power to determine the minimum threshold, i.e. least amount of interrogation power required to activate the RFID chip. Once the RFID chip is activated and selected, it modulates the data in EPC memory and sends the data back to the reader. The measurement resolution by the reader for the interrogation power threshold is 0.1 dBm. Through a USB 2.0 port, a computer interface is used to operate and retrieve measurement data from the reader.

As discussed in the previous section, the antenna sensor is designed with one specific resonance frequency. When the interrogation frequency f by the reader equals the resonance frequency of the sensor, the best impedance matching is achieved between the antenna and the RFID chip. In this scenario, the least amount of power needs to be transmitted by the reader for activating the RFID chip. This means the interrogation power threshold plot $P(f)$ (measured by the reader) reaches minimum value at the resonance frequency. Fig. 8 shows conceptual illustration of resonance frequency shift due to strain. When the antenna size changes, e.g. due to strain/crack, the resonance frequency

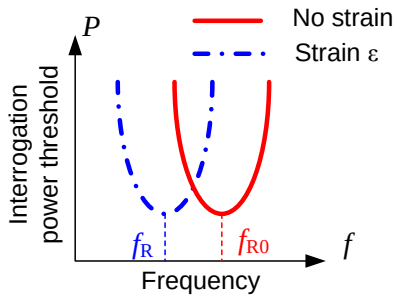

Fig. 8. Conceptual illustration of resonance frequency shift due to strain

changes accordingly to f_R (Eq. (1)), and the $P(f)$ plot for the antenna under strain reaches minimum at f_R. Detailed measurement description can be found in [19].

3. Experiment results on strain sensing

This section first presents tensile test results for wireless strain sensing resolution and maximum measurement range. Strain sensing consistency at longer interrogation distances is then described. Finally, performance of a wireless sensor array is studied. The array consists of three wireless sensors in close proximity.

3.1 Strain sensing resolution

Preliminary study on strain sensing performance of the prototype antenna sensor has been presented in [19], which demonstrates acceptable linearity at 50 με strain steps. In order to investigate

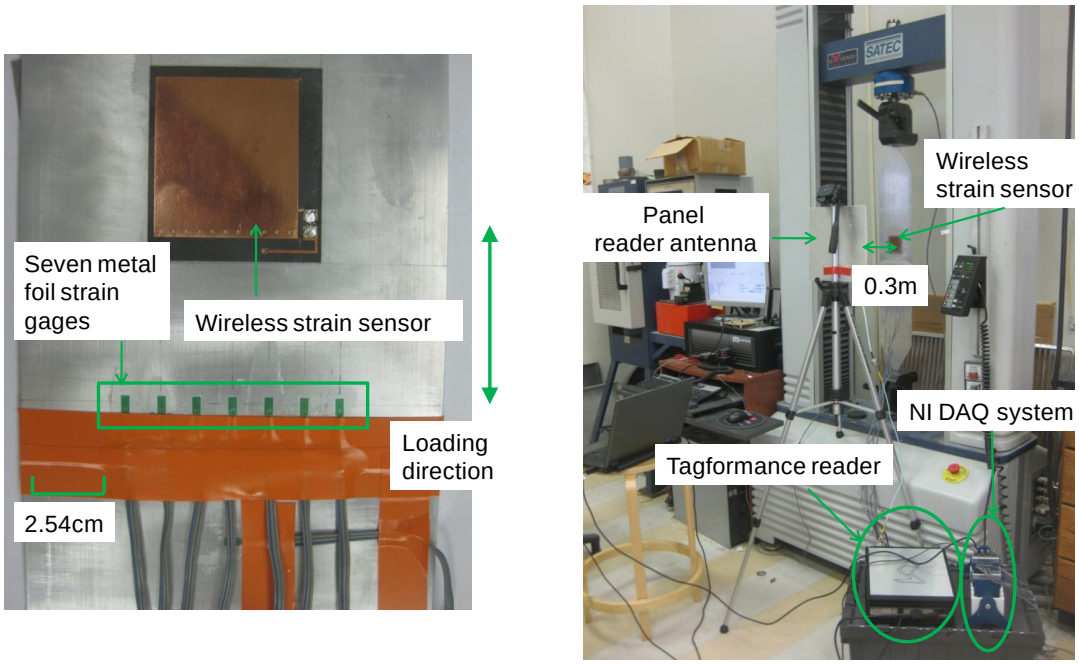

(a) Picture of the sensor instrumentation for wireless sensing experiments

(b) Picture of the experimental setup

Fig. 9. Experimental setup for the tensile tests

the strain sensing resolution limit of the prototype sensor, additional tensile tests are conducted with reduced strain increment per loading step. Fig. 9(a) shows the center area of the tensile testing specimen, with the antenna sensor and seven metal foil strain gages measuring axial strain on the aluminum specimen. The antenna sensor is simply bonded to the specimen by superglue. Fig. 9(b) shows the tensile testing setup with a 100-kN SATEC machine. A Tagformance reader from Voyantic Ltd. is adopted for interrogation power threshold measurement. The panel reader antenna is mounted on a tripod facing the antenna sensor. The distance between the panel antenna and the antenna sensor is set as 0.3m. A National Instruments strain gage module (NI 9235), with a CompactDAQ Chassis (NI cDAQ-9172), is used for collecting data from incorporated metal foil strain gages.

The axial force applied by the 100-kN SATEC machine is configured so that approximately a 20 με strain increment is achieved at each loading step. The test starts with zero strain, and ends at around 200 με. The interrogation power threshold in dBm (dB-milliwatt) scale is measured by the

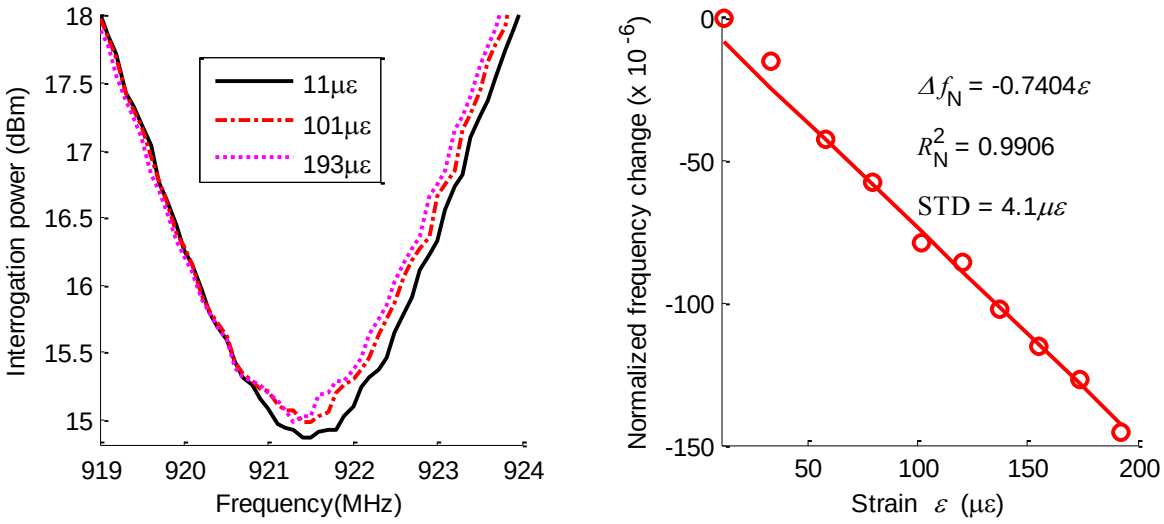

(a) Average interrogation power threshold $P(f)$

(b) Normalized resonance frequency change Δf_N versus strain ε (f_{R0}=921.472 MHz)

Fig. 10. Results for strain sensing resolution at 0.3m interrogation distance

Tagformance reader at each loading step. To reduce the environmental noise effect, five measurements are taken at each strain level and the average interrogation power, $P(f)$, is calculated. Although a total of ten strain levels are tested, for clarity, Fig. 10(a) plots only the average interrogation power threshold at 11 με, 101 με, and 193 με. The strain levels in Fig. 10 are the average value among the seven metal foil strain gages. As described in last section, the interrogation power threshold reaches its minimum value at resonance frequency of the antenna sensor. Fig. 10(a) also shows a clear resonance frequency decrease during strain increase. Since the valley area of the interrogation power threshold plot is relatively flat, a 4th order polynomial curve fitting is performed to the valley area of each plot. The fitted 4th order polynomial is used for identifying the resonance frequency that corresponds to the minimum power [19].

Quality factor of the antenna affects the accuracy in wirelessly identifying antenna resonance frequency. A larger quality factor corresponds to a longer wireless interrogation range, and an increased sharpness of the resonance peak in the interrogation power curve. Eq. (8) shows a general definition of the antenna quality factor [23]:

$$Q_T = \frac{f_R}{\Delta f_{3dB}} \tag{8}$$

where Q_T is the total quality factor of the antenna sensor. The sharpness of the resonance peak in the interrogation power curve is measured by the 3dB bandwidth around the resonance frequency, Δf_{3dB}. According to Eq. (8), the quality factor of the antenna is calculated as 185.3, which indicates a relatively sharp peak in the interrogation power threshold curve.

According to Eq.(6), the normalized frequency change at each strain level is calculated. Fig. 10(b) confirms an approximately linear relationship between the normalized frequency change and strain. Slope of the curve indicates the normalized strain sensitivity, i.e. Δf_N = -0.7404 ppm/με. This means

that 1 με strain increase causes the resonance frequency of the antenna sensor to reduce by 0.7404 ppm. Compared with simulation results in Fig. 6(b), the experimental Δf_N is slightly lower. This is primarily due to strain transfer effect, i.e. only about 90% of the strain on aluminum surface is transferred to top copper layer of the sensor through the 0.787mm thick substrate material Rogers 5880 [19]. The coefficient of determination, R^2, is 0.9906, which indicates acceptable linearity between strain and normalized resonance frequency change. In order to further check the measurement accuracy, the standard deviation of the measurement error is calculated as:

$$STD = \sqrt{\frac{1}{N-1}\sum_{i=1}^{N}\left(\Delta\varepsilon_i\right)^2} \tag{9}$$

where $\Delta\varepsilon_i$ is the difference between measured strain and strain estimated using the linear relationship at the i^{th} strain level; N is the total number of strain levels. Data shown in Fig. 10(b) has a standard deviation is 4.1 με. Although the standard deviation may not be sufficient when high accuracy strain measurement is needed, the results can be acceptable for many applications, particularly when only qualitative evaluation of stress concentration is needed.

3.2 Strain sensing range

Besides strain sensing resolution, maximum strain measurement range is another important performance to be quantified. Similar tensile testing is conducted with a 245-kN MTS-810 machine. To investigate antenna sensor performance at different strain levels, two loading stages are adopted. From 0 to 1,000 με, each loading step is configured to increase the strain level by about 100 με. From 1,000 με to 10,000 με, each loading step generates a strain increment of about 1,000 με. In total, twenty-six strain levels are tested. Other experimental setups and data processing remain the same as before.

Fig. 11(a) shows the average interrogation power threshold plot measured at different strain levels. For clarity, only five example strain levels are shown in the figure. Decrease in resonance frequency is observed when strain increases. The normalized resonance frequency change Δf_N is plotted for all twenty-six strain levels in Fig. 11(b). From power threshold plots, resonance frequency is determined for each strain level. Linear regression is performed separately to three segments of the plot in Fig. 11(b). For segment ① with data points from 0 to 1,000 με, the normalized strain sensitivity is -0.7542 ppm/με, and the coefficient of determination is 0.9974. For segment ② with data points from 1,000 to 4,500 με, the normalized strain sensitivity is -0.7784 ppm/με, which is very close to the result in segment ①. The slight difference can be explained by Eq. (1), which shows that the approximate linearity between resonance frequency and strain becomes weaker as strain becomes larger. For segment ③, the normalized strain sensitivity is reduced to -0.382 ppm/με. This is obviously caused by the yielding of both the aluminum specimen and the copper antenna, as well as the dielectric property change of the Rogers 5880 substrate. Determination coefficient for the third

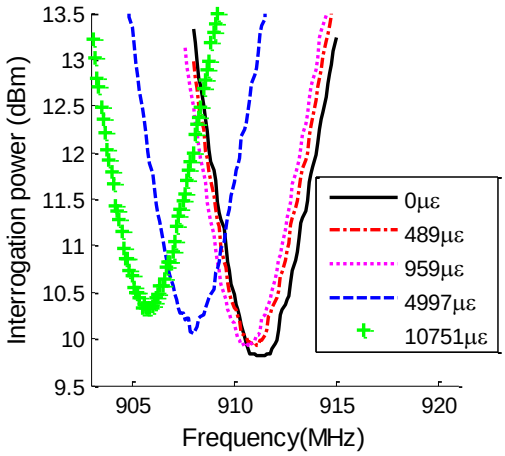

(a) Average interrogation power threshold $P(f)$

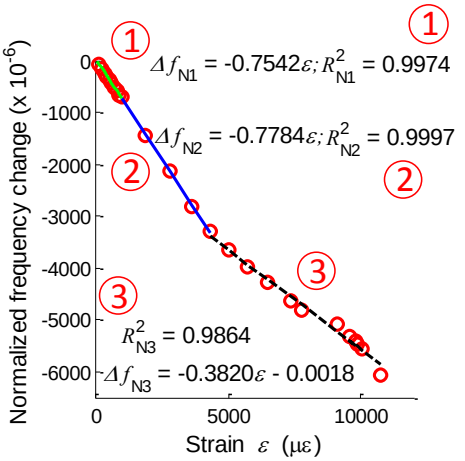

(b) Normalized frequency change Δf_N versus strain ε (f_{R0}=911.407 MHz)

Fig. 11. Results for strain sensing range at 0.3m interrogation distance

segment is smaller than the first two segments, because material property becomes more non-linear.

3.3 Strain sensing consistency at different interrogation distances

Interrogation distance between the reader antenna and a prototype antenna sensor is critical for field deployment. This section describes the strain sensing consistency of an antenna sensor at different interrogation distances. The experimental setup is shown in Fig. 12. During this experiment, the reader antenna is changed to an 18 dBi high-gain Yagi antenna (APX-ANT-0918 from Technology Hardware & Resources). With a high-gain reader antenna, less interrogation power is required in order to active the RFID chip. On the other hand, the interrogation distance can be improved at the same interrogation power. Two different interrogation distances, 1.5m and 2.1m, are tested for comparison. The tensile load is configured so that approximately 50 με increment is achieved at each loading step. All other experimental setups and data analysis remain the same as before.

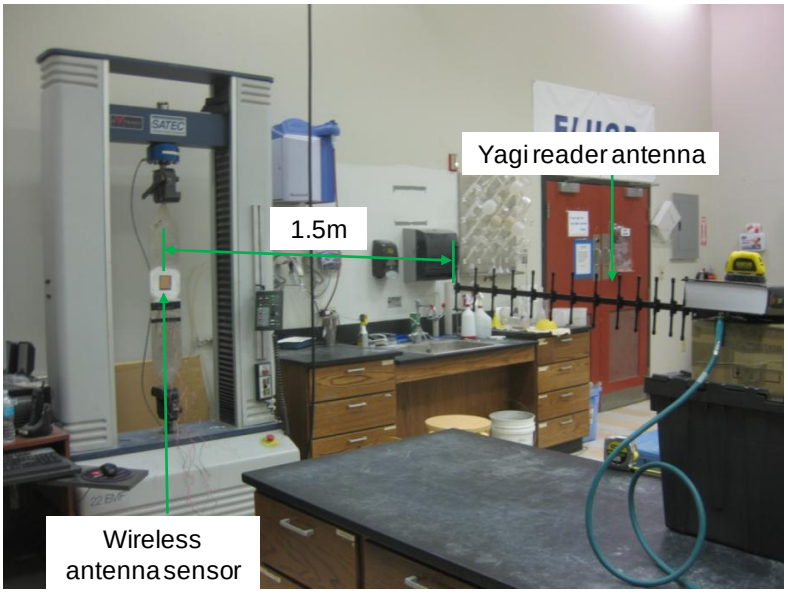

Fig. 12. Experimental setup for a tensile test with 1.5m interrogation distance

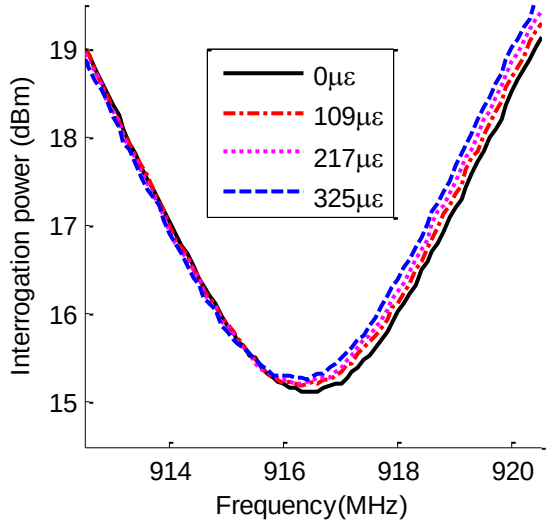

(a) Average interrogation power threshold $P(f)$

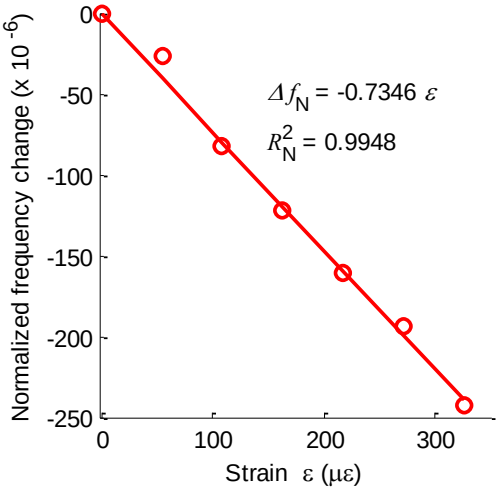

(b) Normalized resonance frequency change Δf_N versus strain ε (f_{R0}=916.455 MHz)

Fig. 13. Tensile testing results at 1.5m interrogation distance

The interrogation power threshold plots for two interrogation distances are shown in Fig. 13 and Fig. 14, respectively. Seven strain levels are tested at each distance. For clarity, interrogation power threshold plots for only four strain levels are illustrated in Fig. 13(a) and Fig. 14(a). Fig. 13(b) shows

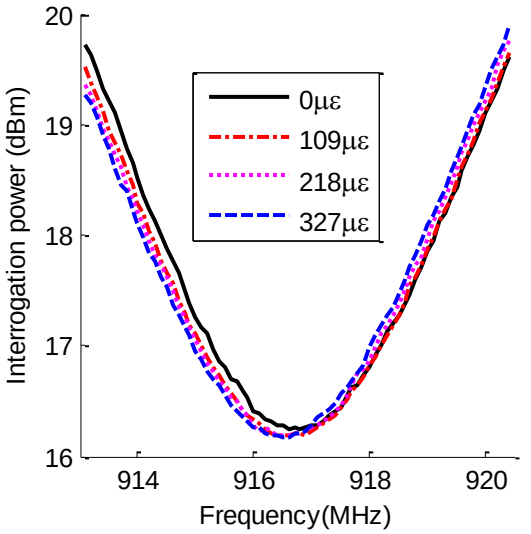

(a) Average interrogation power threshold $P(f)$

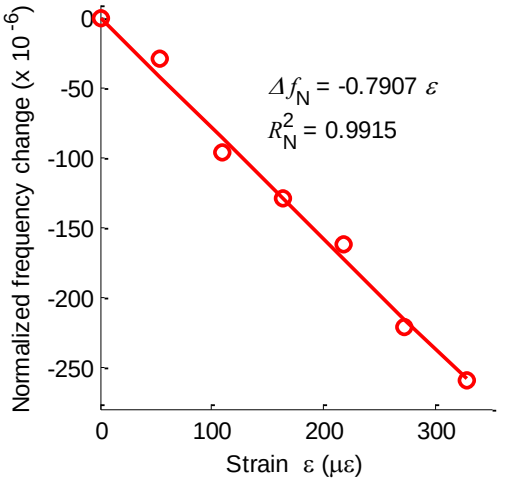

(b) Normalized resonance frequency change Δf_N versus strain ε (f_{R0}=916.738 MHz)

Fig. 14. Tensile testing results at 2.1m interrogation distance

the normalized strain sensitivity is -0.7346 ppm/με when the interrogation distance is 1.5m. Similarly, Fig. 14(b) shows normalized strain sensitivity is -0.7907 ppm/με for 2.1m interrogation distance. The corresponding coefficients of determination for these two cases are 0.9948 and 0.9915, which indicate acceptable linearity. Nevertheless, future work is needed to further improve strain sensitivity consistency at different interrogation distances.

3.4 Wireless antenna sensor array

Besides harvesting electromagnetic power from the interrogation signal emitted by the reader, the RFID chip allows operation of multiple sensors in close proximity through its identification mechanism. The RFID chip integrated in the prototype sensor contains a 240-bit electronic product code (EPC) memory, which is utilized for identification among multiple sensors. The performance of a three-sensor array is investigated. Fig. 15(a) shows the center area of the aluminum specimen, where three antenna sensors and four metal foil strain gages are installed. Fig. 15(b) shows the experimental setup for tensile testing. A panel antenna is placed 0.3m away from the specimen, facing the middle antenna sensor. Testing load is configured so that approximately 50με increment is achieved at each loading step. A LabVIEW program is implemented for the reader to activate one sensor at a time, using a unique identification code written to the EPC memory of every RFID chip following Class-1 Generation-2 UHF RFID protocol [25]. Only one selected sensor actively responds and communicates with the reader at a time.

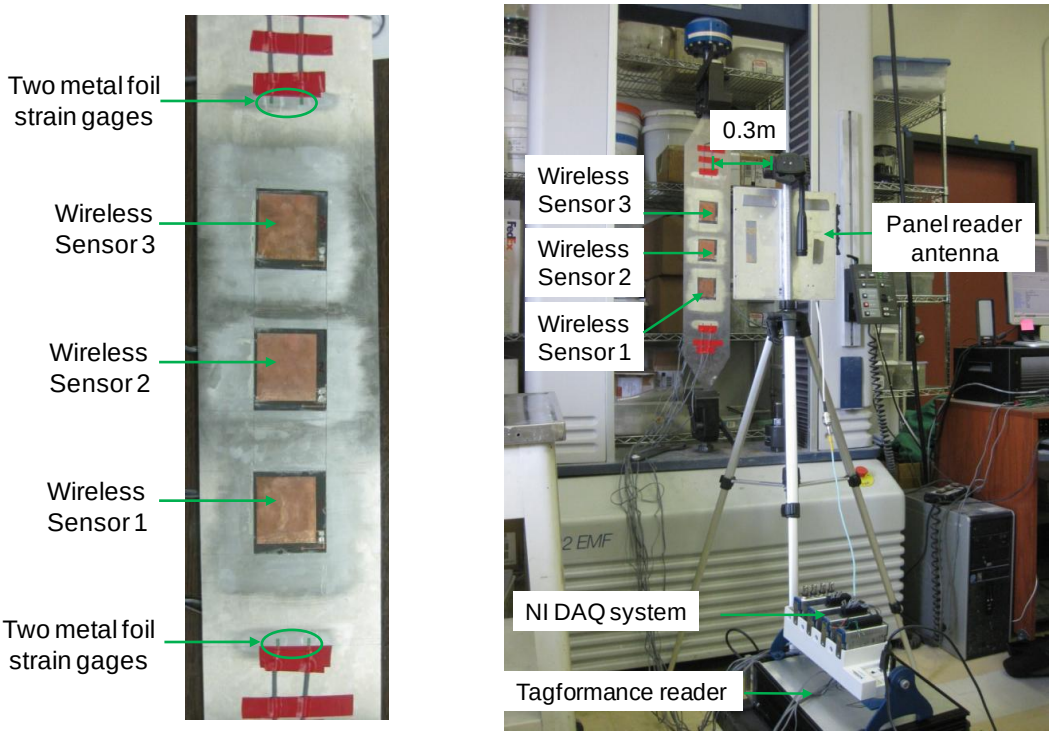

(a) Wireless sensor array on an aluminum specimen

(b) Experimental setup

Fig. 15. Experimental setup for the tensile test with a wireless sensor array

The average interrogation power thresholds of three sensors are plotted in Fig. 16(a), Fig. 17(a), and Fig. 18(a) for four example strain levels. For clarity, only four strain levels are shown in each interrogation power threshold plots. Resonance frequency shift is observed for all three sensors when strain increases. Normalized resonance frequency change is plotted against strain in Fig. 16(b), Fig. 17(b), and Fig. 18(b). The three normalized strain sensitivities are -0.7277 ppm/με, -0.7198 ppm/με, and -0.7264 ppm/με. The similarity among three sensitivities indicates that the antenna sensors can operate in close proximity with little electromagnetic interference. The normalized strain sensitivities in sensor array testing are also close to the sensitivity values from previous single sensor tests.

Although the results are overall promising, certain interference among neighboring sensors still

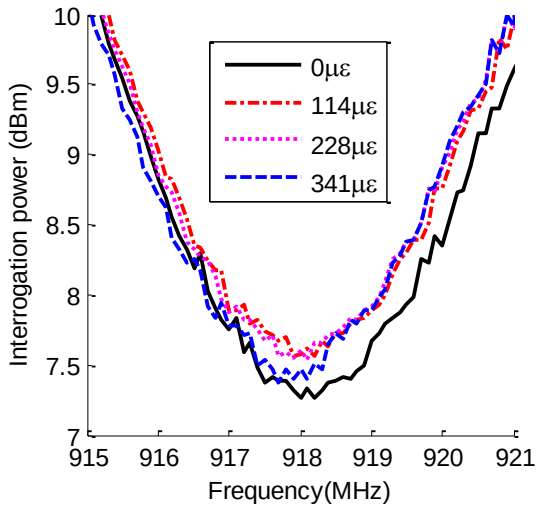

(a) Average interrogation power threshold $P(f)$

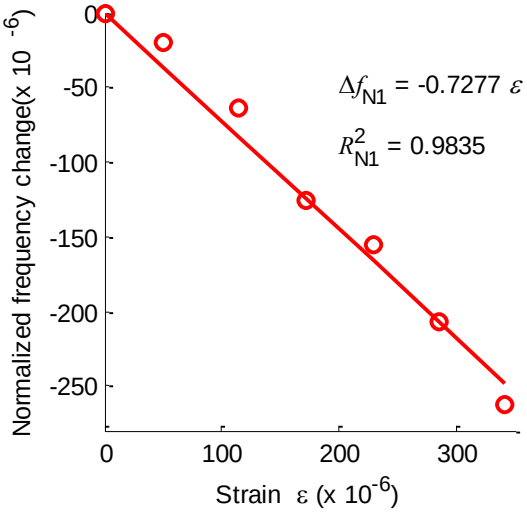

(b) Normalized resonance frequency change Δf_N versus strain ε (f_{R0}=918.127 MHz)

Fig. 16. Tensile testing results for Sensor 1

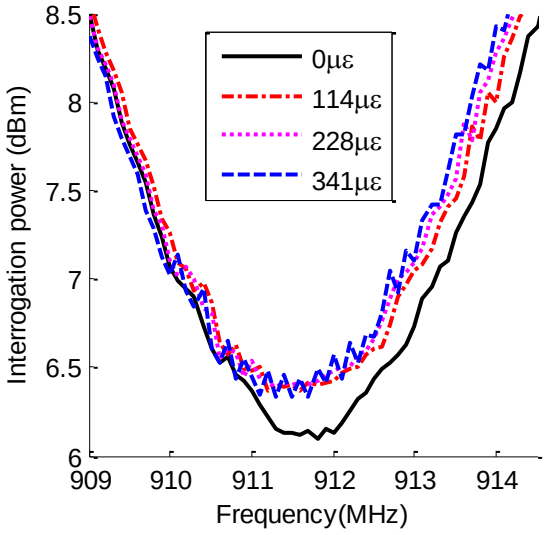

(a) Average interrogation power threshold $P(f)$

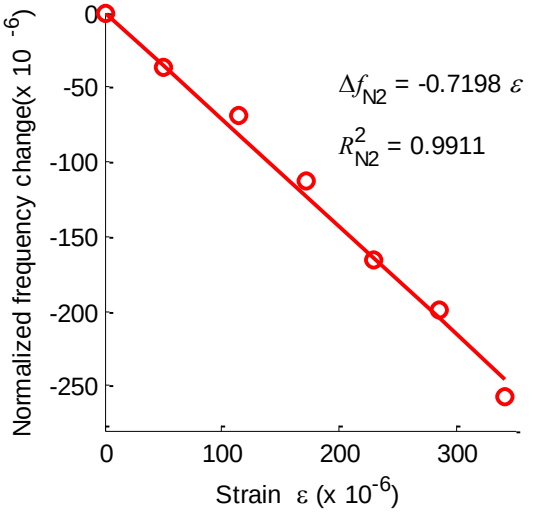

(b) Normalized resonance frequency change Δf_N versus strain ε (f_{R0}=911.611 MHz)

Fig. 17. Tensile testing results for Sensor 2

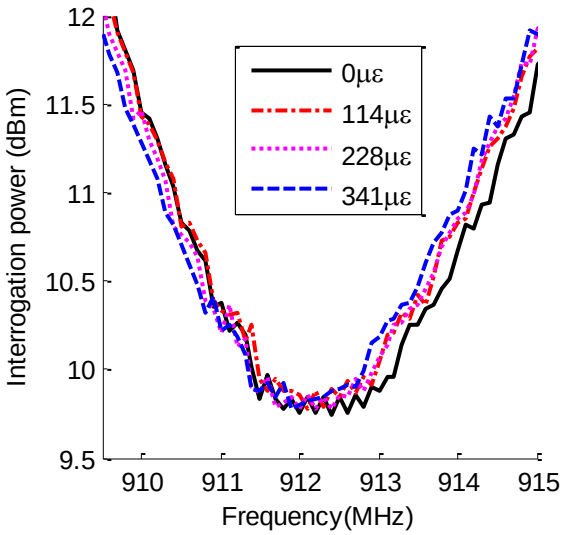

(a) Average interrogation power threshold $P(f)$

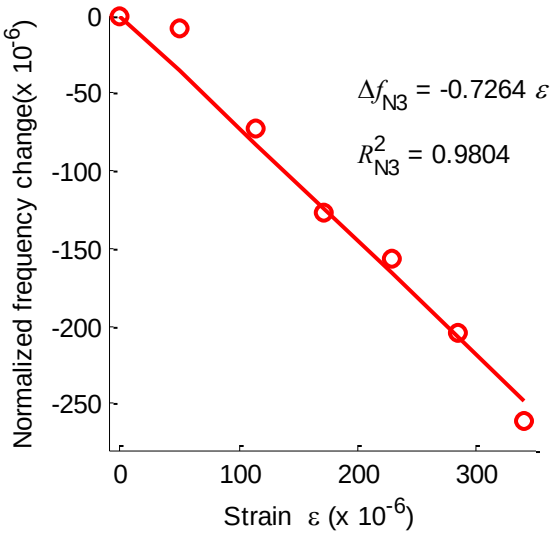

(b) Normalized resonance frequency change versus strain ε (f_{R0}=912.326 MHz)

Fig. 18. Tensile testing results for Sensor 3

exists. This is clearly demonstrated by the more zigzag interrogation power threshold plots for sensor array testing as compared with single sensor testing. Even though only the selected RFID sensor responds to the reader with modulated signals, other RFID antennas still passively reflect un-modulated electromagnetic reflection to the reader. Because all three RFID antennas have close resonance frequencies, the electromagnetic reflection causes inevitable interference. Future study is needed to reduce the interference, for example, by designing antenna sensors with somewhat different initial resonance frequencies at zero strain level. Nevertheless, current sensor performance can be adequate for a qualitative measurement of stress concentration when small inaccuracies are acceptable.

4. Experimental results on crack sensing

Crack sensing performance of the prototype antenna sensor is described in this section. A crack testing device is first designed to emulate crack opening. The crack sensing performance of the

antenna sensor is evaluated using emulated crack opening. Fatigue crack test of the antenna sensor is also performed, using a standard compact-tension specimen.

4.1 Emulated crack testing

To conveniently emulate crack propagation, a special crack testing device (Fig. 19(a)) is designed for the experiments. The crack testing device consists of three aluminum plates, i.e. a base plate (41cm × 30cm × 2.5cm), a rotating top plate (20cm × 10cm × 1.3cm), and a fixed bottom plate (20cm × 10cm × 1.3cm). Due to their thickness, all three plates can be assumed to remain rigid during crack testing for the sensor. The fixed bottom plate is fastened to the base plate by four corner bolts. The rotating top plate is attached to the base plate by one bolt at the bottom right corner, which acts as the rotation axis. A fine-resolution displacement control screw (1mm threading) is installed at the top left corner of the

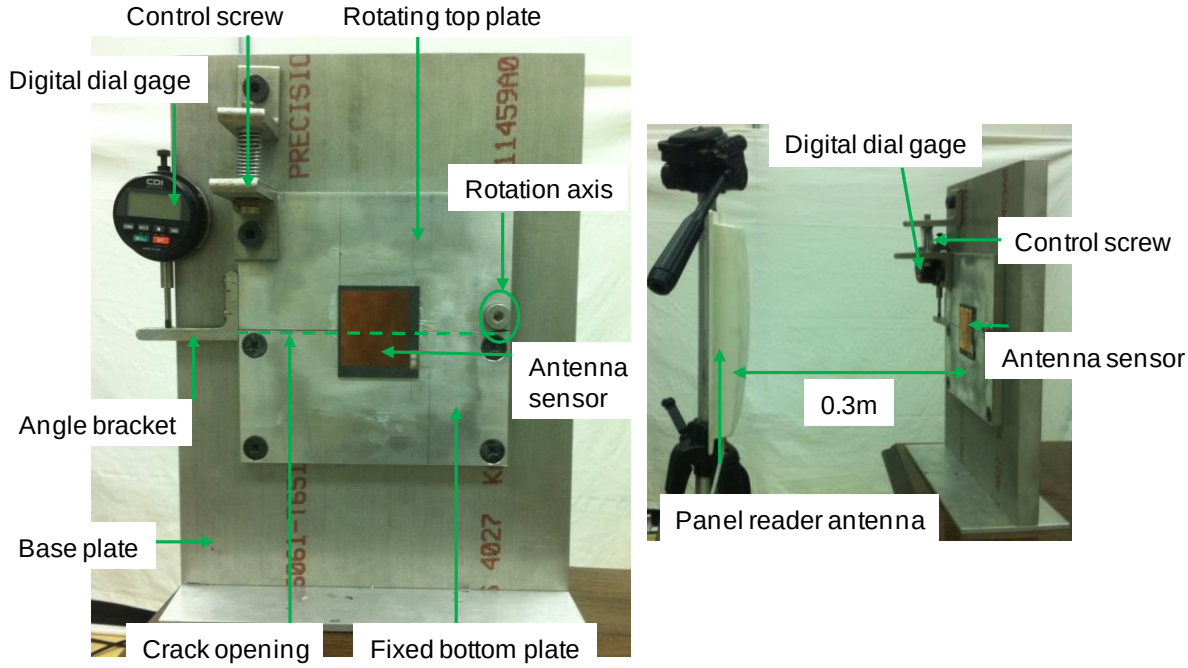

(a) Photo of the crack testing device (b) Experimental setup

Fig. 19. Experimental setup of emulated crack test

rotating plate. By turning the screw, a rotation is imposed on the top plate and a crack/gap is opened between the top and bottom plates, as marked by the dash line in Fig. 19(a). The crack opening size is measured by a digital dial gage (2.54×10^{-6} m resolution) mounted at the left side of the base plate. A spring-loaded probe from the gage pushes against an angle bracket that is fastened to the left edge of the rotating plate.

For crack sensing, the back side of a prototype antenna sensor is bonded on the rotating and fixed plates, above the gap and at the center of the crack opening line. The experimental setup for wireless interrogation is shown in Fig. 19(b). The panel reader antenna faces the center of the prototype sensor at a distance of 0.3m. Through a coaxial cable, the reader antenna is connected with the Tagformance reader unit. At each crack opening size, the Tagformance reader sweeps through a frequency range to measure the interrogation power threshold, so that the resonance frequency of the antenna sensor can be determined. After the reader finishes interrogation at one crack opening size, the displacement control screw is turned to reach the next crack opening size.

Fig. 20 shows representative photos of the deformed/cracked antenna sensor at three different crack opening sizes. Crack size underneath the sensor is estimated from dial gage reading. Fig. 20 (a) shows

(a) 0.13m (b) 0.53mm (c) 0.81mm

Fig. 20. Photos of deformed antenna sensor at different crack opening sizes

the sensor at 0.13mm crack opening. No fracture occurs on the sensor, but slight deformation is observed on the top copper cladding. Fig. 20 (b) shows when crack opening is 0.53mm, which is the last strain level when the RFID sensor responds. Small fractures have developed on the top copper and the substrate, but the sensor still functions properly. The loading step after 0.53mm causes rapid breakage of the sensor, as shown in Fig. 20 (c). At this point, the crack grows through the entire antenna width. No response from the antenna sensor can be received by the Tagformance reader. In total, fourteen crack opening sizes are wirelessly measured during the experiment. For clarity, Fig. 21(a) shows the interrogation power threshold plots for only five crack opening sizes. It is observed that the antenna resonance frequency reduces gradually when crack opening increases the normalized resonance frequency change is plotted against crack opening size in Fig. 21(b). A linear regression is performed on the fourteen data points. The slope of -1.19×10^4 ppm/mm represents the emulated crack sensing sensitivity, which means 1 mm crack underneath the sensor causes the resonance frequency to reduce by 1.19×10^4 ppm.

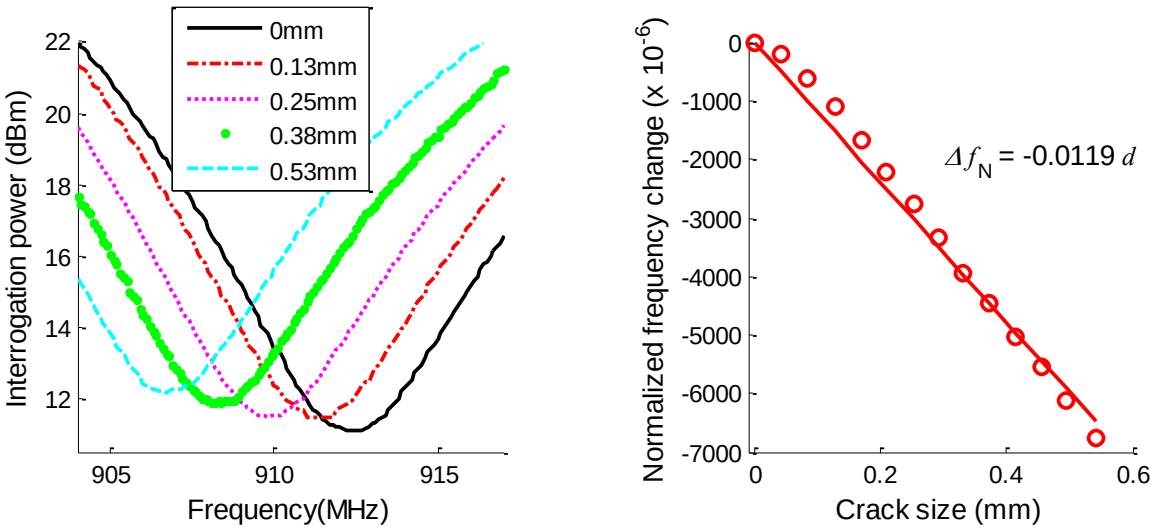

(a) Average interrogation power threshold $P(f)$

(b) Normalized frequency change Δf_N versus crack opening d (f_{R0}=912.822 MHz)

Fig. 21. Experimental results for emulated crack test

Because the aluminum plates in Fig. 19 remain fairly rigid during the testing, crack opening in the testing is much simplified as compared to an actual fatigue crack that occurs on a structure in the field. However, it should be noted that as shown in Fig. 20, the sensor still experiences a complicated deformation process. At the beginning of the experiment, crack opening generated by the rotating plate causes stress concentration along the center line of the sensor ground plane, i.e. bottom copper layer. The strain/deformation also propagates through the substrate and into the top copper layer. When the crack opening increases to a certain point, fracture in the bottom copper starts, and gradually propagates to fracture in the substrate and top copper near the end of the testing. Although accurate measurement of bottom copper fracture is difficult to obtain, it is likely that most of the observed resonance frequency shift is caused by antenna strain/deformation, instead of by antenna fracture.

4.2 Fatigue crack testing

To characterize sensor performance measuring fatigue crack, a compact-tension (CT) specimen is designed and fabricated according to ASTM standard E647-11. Fig. 22(a) shows the design drawing

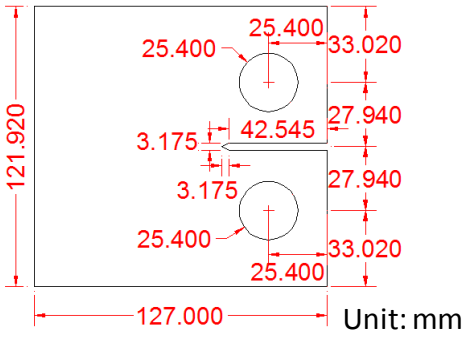

(a) Design drawing of fatigue specimen

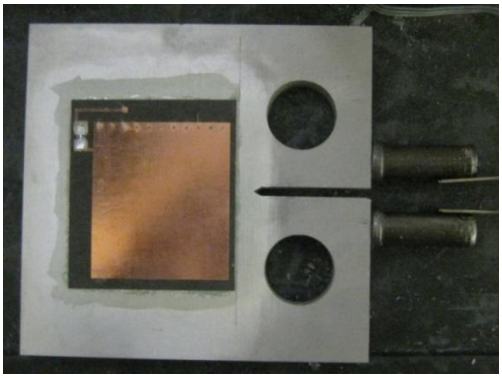

(b) Fatigue specimen together with prototype antenna sensor

Fig. 22. Design drawing and photo of a fatigue test specimen

of the fatigue test specimen, and Fig. 22(b) shows a photo of the fatigue specimen made of Aluminum 6061-T651. A prototype sensor is installed at the central area of the 12.7cm × 12.2cm ×1.3cm specimen. Experimental setup for the fatigue test is shown in Fig. 23. An extensometer is installed at the notch side of the specimen to measure crack opening width. Besides crack width measurement, crack length on the back of the CT specimen is measured. To identify crack tip location, dye penetrant is sprayed on the back surface for measuring crack length with a caliper. After a pre-crack is generated, the specimen is subject to 5 Hz cyclic loading. A loading ratio R= P_{max}/P_{min}=0.5 is adopted. The loading level is determined by crack growth rate. In this test, the minimum and maximum load are 8.9kN and 17.8kN, respectively, to provide a crack growth rate that results in a reasonable experiment duration. After every 10,000 cycles of loading, the specimen is held at 13.3 kN static load for wireless interrogation. Resonance frequency of the antenna sensor is interrogated by the Tagformance reader, with a panel reader antenna placed at 0.3m away from the sensor. The specimen is broken apart after 110,000 cycles, which takes about 6 hours in total. Fig. 24(a) and Fig. 24(b) show photos of the front and back view of the specimen after 90,000 cycles. As shown in Fig. 24(b), the crack length after 90,000 cycles is 24.3mm. Fig. 24(c) and Fig. 24(d) show the front and back view of the failed specimen.

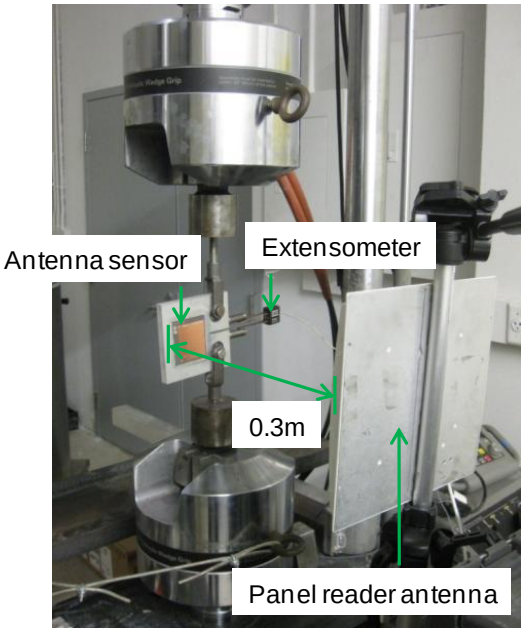

Fig. 23 Experiment setup for fatigue test

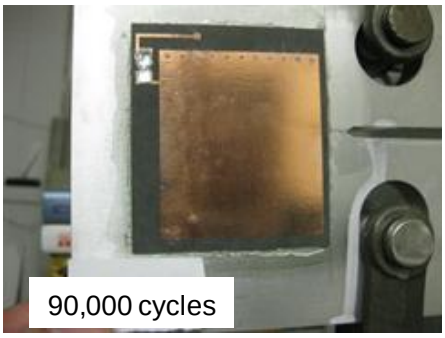

(a) Front view

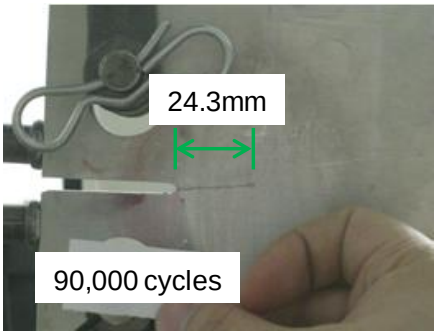

(b) Back view

(c) Front view of the failed specimen

(d) Back view of the failed specimen

Fig. 24. Failed specimen photo

Fig. 25(a) shows average interrogation power threshold at different crack lengths. Although measurements are obtained for ten different lengths, for clarity, plots for only four crack lengths are shown in Fig. 25(a). About 2MHz resonance frequency decrement is observed when the crack length increases to 24.3mm. Normalized resonance frequency changes at all crack lengths are shown in Fig. 25(b). Resonance frequency of the antenna sensor keeps decreasing when crack length increases. At the last time when wireless measurement can still be obtained, crack length grows to 33mm. The final obtained resonance frequency drops down to 867.6MHz (i.e. 5.37% decrease in normalized resonance frequency). To make the trend in other points distinguishable, Fig. 25(b) does not show this final data point. Compared with the emulated crack testing result shown in Fig. 21(b), much less linearity is observed in fatigue testing data. This is because more complicated deformation occurs in the sensor during fatigue testing, where stress concentration is highly localized around the crack tip. More quantitative studies, possibly through multi-physics simulation, can be performed in the future to investigate the phenomenon in detail.

5. Summary and Discussion

This paper presents the latest simulation and experimental results of a wireless and passive (battery-free) RFID antenna sensor for strain/crack sensing. Electromagnetic simulation is performed to evaluate strain sensing performance of the sensor. A strong linearity is illustrated between simulated resonance frequency shift and strain. The corresponding normalized strain sensitivity is -0.8927 ppm/με. Validation experiments are conducted to characterize strain measurement resolution and range. Test results show that the antenna sensor can measure strain as small as 20 με and as high as 10,000 με. Using a Yagi reader antenna, the antenna sensor can achieve consistent strain sensing

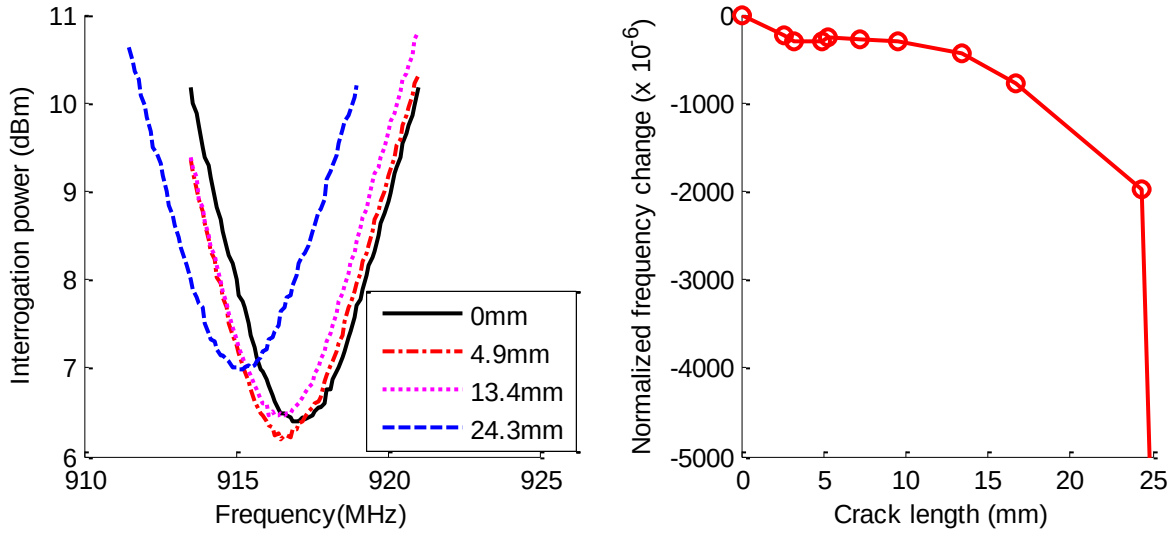

(a) Average interrogation power threshold $P(f)$

(b) Normalized frequency change Δf_N versus crack size d (f_{R0}=913.184 MHz)

Fig. 25. Experimental results for fatigue test

results when the interrogation distance is increased up to 2.1m. In addition, a sensor array formed by three antenna sensors is capable of measuring strain distribution in close proximity. At last, two scenarios of crack sensing performance are also presented, including emulated crack sensing and fatigue crack sensing. The experimental results demonstrate that the antenna sensor is capable of measuring sub-millimeter crack and tracking crack propagation.

Since the resonance frequency of the antenna sensor is related with physical dimension of the sensor dimension can be reduced by increasing operating frequency of the antenna sensor. Meanwhile, the absolute strain sensing sensitivity can be increased when the operating frequency of the sensor is increased, according to Eq. (1). Future research needs to be performed to improve sensing consistency at different interrogation distances. For example, higher strain sensitivity and higher received power increase received signal strength and thus improve strain sensing consistency. To this end, high sensitivity sensors and power amplifier at the sensor side can be promising solutions. Furthermore, the

sensing interference between sensors in close proximity is another topic that requires more investigation. Sensor placement needs to be optimized in order to improve signal-to-noise ratios. Another way to reduce the interference is to differentiate initial resonance frequency f_{R0} of sensors in close proximity. This approach allows each sensor to change its resonance frequencies within a different range, and thus minimizes interference. In addition, performance of the sensor under different crack propagation scenarios can be studied, such as the propagation and coalescence of multiple cracks. Finally, while this study focuses upon application on steel structure surface, sensor performance can be investigated when the sensor is embedded inside concrete.

ACKNOWLEDGMENT

This material is based upon work supported by the Federal Highway Administration under agreement No. DTFH61-10-H-00004. Any opinions, findings, and conclusions or recommendations expressed in this publication are those of the authors and do not necessarily reflect the view of the Federal Highway Administration. In addition, the authors would like to acknowledge the assistance with the experimental testing provided by Mr. Chia-Hung Fang and Mr. Gabriel Lantz.

6. REFERENCES

[1] H. Sohn, C. R. Farrar, F. M. Hemez, D. D. Shunk, D. W. Stinemates, and B. R. Nadler, *A Review of Structural Health Monitoring Literature: 1996-2001*. Los Alamos National Laboratory, Los Alamos, NM Report No. LA-13976-MS, 2003.

[2] M. Çelebi, *Seismic Instrumentation of Buildings (with Emphasis on Federal Buildings)*. United States Geological Survey, Menlo Park, CA Report No. 0-7460-68170, 2002.

[3] E. G. Straser and A. S. Kiremidjian, *A Modular, Wireless Damage Monitoring System for Structures*. John A. Blume Earthquake Eng. Ctr., Stanford University, Stanford, CA Report No. 128, 1998.

[4] B. F. Spencer, Jr., M. E. Ruiz-Sandoval, and N. Kurata, "Smart sensing technology: opportunities and challenges," *Structural Control and Health Monitoring*, vol. 11, pp. 349-368, 2004.

[5] J. P. Lynch, K. H. Law, A. S. Kiremidjian, C. E., C. R. Farrar, H. Sohn, D. W. Allen, B.

Nadler, and J. R. Wait, "Design and performance validation of a wireless sensing unit for structural health monitoring applications," *Structural Engineering and Mechanics*, vol. 17, pp. 393-408, 2004.

[6] Y. Wang, J. P. Lynch, and K. H. Law, "A wireless structural health monitoring system with multithreaded sensing devices: design and validation," *Structure and Infrastructure Engineering*, vol. 3, pp. 103-120, 2007.

[7] J. P. Lynch and K. J. Loh, "A summary review of wireless sensors and sensor networks for structural health monitoring," *The Shock and Vibration Digest*, vol. 38, pp. 91-128, 2006.

[8] G. Park, T. Rosing, M. D. Todd, C. R. Farrar, and W. Hodgkiss, "Energy harvesting for structural health monitoring sensor networks," *Journal of Infrastructure Systems*, vol. 14, pp. 64-79, 2008.

[9] K. Finkenzeller, *RFID Handbook*. 2nd ed. New York: John Wiley & Sons, 2003.

[10] F. Gasco, P. Feraboli, J. Braun, J. Smith, P. Stickler, and L. DeOto, "Wireless strain measurement for structural testing and health monitoring of carbon fiber composite," *Composite Part A: Applied Science and Manufacturing*, vol. 42, pp. 1263-1274, 2011.

[11] J. C. Butler, A. J. Vigliotti, F. W. Verdi, and S. M. Walsh, "Wireless, passive, resonant-circuit, inductively coupled, inductive strain sensor," *Sensors and Actuators A: Physical*, vol. 102, pp. 61-66, 2002.

[12] K. J. Loh, J. P. Lynch, and N. A. Kotov, "Inductively coupled nanocomposite wireless strain and pH sensors," *Smart Structures and Systems*, vol. 4, pp. 531-548, 2008.

[13] Y. Jia, K. Sun, F. J. Agosto, and M. T. Quinones, "Design and characterization of a passive wireless strain sensor," *Measurement Science and Technology*, vol. 17, pp. 2869-2876, 2006.

[14] A. Daliri, A. Galehdar, S. John, C. H. Wang, W. S. T. Towe, and K. Ghorbani, "Wireless strain measurement using circular microstrip patch antennas," *Sensors and Actuators A: Physical*, vol. 184, pp. 86-92, 2012.

[15] S. Deshmukh and H. Huang, "Wireless interrogation of passive antenna sensors," *Measurement Science and Technology*, vol. 21, 2010.

[16] X. Xu and H. Huang, "Battery-less wireless interrogation of microstrip patch antenna for strain sensing," *Smart Materials and Structures*, vol. 21, p. 125007, 2012.

[17] D. J. Thomson, D. Card, and G. E. Bridges, "RF cavity passive wireless sensors with time-domain gating-based interrgoation for SHM of civil structures," *Sensors Journal, IEEE*, vol. 9, pp. 1430-1438, 2009.

[18] C. Occhiuzzi, C. Paggi, and G. Marrocco, "Passive RFID strain-sensor based on meander-line antennas," *IEEE Transactions on Antennas and Propagation*, vol. 59, pp. 4836-4840, 2011.

[19] X. Yi, T. Wu, Y. Wang, R. T. Leon, M. M. Tentzeris, and G. Lantz, "Passive wireless smart-skin sensor using RFID-based folded patch antennas," *International Journal of Smart and Nano Materials*, vol. 2, pp. 22-38, 2011.

[20] X. Yi, T. Wu, G. Lantz, Y. Wang, R. T. Leon, and M. M. Tentzeris, "Thickness variation study of RFID-based folded patch antennas for strain sensing," in *Proceedings of SPIE, Sensors and Smart Structures Technologies for Civil, Mechanical and Aerospace Systems*, San Diego, CA, USA, 2011.

[21] X. Yi, R. Vyas, C. Cho, C.-H. Fang, J. Cooper, Y. Wang, R. T. Leon, and M. M. Tentzeris, "Thermal effects on a passive wireless antenna sensor for strain and crack sensing," in *Proceedings of SPIE, Sensors and Smart Structures Technologies for Civil, Mechanical and Aerospace Systems*, San

Diego, CA, USA, 2012.

[22] D. M. Pozar, *Microwave Engineering*. 3rd ed. New York: John Wiley & Sons, Inc., 2005.

[23] C. A. Balanis, *Antenna Theory: Analysis and Design*. 3rd ed. New York: John Wiley & Sons, 2005.

[24] Voyantic Ltd., *Tagformance Measurement System Manual*. Voyantic Ltd., Espoo, Finland Rev 3.8.x, 2011.

[25] EPCglobal Inc., *EPC™ Radio-frequency Identity Protocols Class-1 Generation-2 UHF RFID Protocol for Communications at 860 MHz-960 MHz* EPCglobal Inc. Version 1.2.0, 2008.